

Oxygen abundance distributions in six late-type galaxies based on SALT spectra of H II regions^{*}

I. A. Zinchenko^{1,2}, A. Y. Kniazev^{3,4,5}, E. K. Grebel¹, and L. S. Pilyugin^{1,2,6}

¹ Astronomisches Rechen-Institut, Zentrum für Astronomie der Universität Heidelberg, Mönchhofstr. 12–14, 69120 Heidelberg, Germany

² Main Astronomical Observatory, National Academy of Sciences of Ukraine, 27 Akademika Zabolotnoho St., 03680, Kyiv, Ukraine

³ South African Astronomical Observatory, PO Box 9, 7935 Observatory, Cape Town, South Africa

⁴ Southern African Large Telescope Foundation, PO Box 9, 7935 Observatory, Cape Town, South Africa

⁵ Sternberg Astronomical Institute, Lomonosov Moscow State University, Universitetskij Pr. 13, Moscow 119992, Russia

⁶ Kazan Federal University, 18 Kremlyovskaya St., 420008, Kazan, Russian Federation

Preprint online version: September 21, 2018

ABSTRACT

Spectra of 34 H II regions in the late-type galaxies NGC 1087, NGC 2967, NGC 3023, NGC 4030, NGC 4123, and NGC 4517A were observed with the South African Large Telescope (SALT). In all 34 H II regions, oxygen abundances were determined through the “counterpart” method (*C* method). Additionally, in two H II regions in which the auroral lines were detected oxygen abundances were measured through the classic T_e method. We also estimated the abundances in our H II regions using the O3N2 and N2 calibrations and compared those with the *C*-based abundances. With these data we examined the radial abundance distributions in the disks of our target galaxies. We derived surface-brightness profiles and other characteristics of the disks (the surface brightness at the disk center and the disk scale length) in three photometric bands for each galaxy using publicly available photometric imaging data. The radial distributions of the oxygen abundances predicted by the relation between abundance and disk surface brightness in the *W1* band obtained for spiral galaxies in our previous study are close to the radial distributions of the oxygen abundances determined from the analysis of the emission line spectra for four galaxies where this relation is applicable. Hence, when the surface-brightness profile of a late-type galaxy is known, this parametric relation can be used to estimate the likely present-day oxygen abundance in its disk.

Key words. galaxies: abundances – ISM: abundances – H II regions, galaxies: individual: NGC 1087, NGC 2967, NGC 3023, NGC 4030, NGC 4123, NGC 4517A

1. Introduction

Metallicities play a key role in studies of galaxies. The present-day abundance distributions across a galaxy provide important information about the evolutionary status of that galaxy and form the basis for the construction of models of the chemical evolution of galaxies.

Oxygen abundances and their gradients in the disks of late-type galaxies are typically based on emission-line spectra of individual H II regions. When the auroral line [O III] λ 4363 is detected in the spectrum of an H II region, the T_e -based oxygen $(O/H)_{T_e}$ abundance can be derived using the standard equations of the T_e -method. In our current study, we do not always have this information and use alternative methods where the auroral line is not detected. In those cases, we estimate the oxygen abundances from strong emission lines using a recently suggested method (called the “*C* method”) for abundance determinations of Pilyugin et al. (2012) and Pilyugin et al. (2014a). When the strong lines R_3 , N_2 , and S_2 are measured in the spectrum of an H II region, the oxygen $(O/H)_{C_{SN}}$ abundance can be determined. When the strong lines R_2 , R_3 , and N_2 are measured in the spectrum, we can measure the oxygen $(O/H)_{C_{ON}}$ abundance.

It should be emphasized that the *C* method produces abundances on the same metallicity scale as the T_e -method. In contrast, metallicities derived using one of the many calibrations based on photoionization models tend to show large discrepancies (of up to ~ 0.6 dex) with respect to T_e -based abundances (see the reviews by Kewley & Ellison 2008; López-Sánchez & Esteban 2010; López-Sánchez et al. 2012). Coupling our emission-line measurements with available line measurements from the literature or public databases, we measured the radial distributions of the oxygen abundances across the disks of six galaxies.

The study of the correlations between the oxygen abundance and other properties of spiral and irregular galaxies is important for understanding the formation and evolution of galaxies. The correlation between the local oxygen abundance and the stellar surface brightness (the OH – *SB* relation) or surface mass density has been a subject of discussion for a long time (Webster & Smith 1983; Edmunds & Pagel 1984; Vila-Costas & Edmunds 1992; Ryder 1995; Moran et al. 2012; Rosales-Ortega et al. 2012; Sánchez et al. 2014). We examined the relations between the oxygen abundance and the disk surface brightness in the infrared *W1* band at different fractions of the optical isophotal radius R_{25} in our previous paper (Pilyugin et al. 2014b). *W1* is the photometric band of the *Wide-field Infrared Survey Explorer (WISE)*; see Wright et al. (2010). We found evidence that the OH – *SB* relation depends on the

^{*} Based on observations made with the Southern African Large Telescope, programs 2012-1-RSA_OTH-001, 2012-2-RSA_OTH-003 and 2013-1-RSA_OTH-005.

galactocentric distance (taken as a fraction of the optical radius R_{25}) and on other properties of a galaxy, namely its disk scale length and the morphological T -type. In that study, we suggested a parametric OH – SB relation for spiral galaxies.

In our current paper, we present results from observations of emission-line spectra of H II regions in six spiral galaxies. These observations were obtained with the South African Large Telescope as a part of our investigation of the abundance properties of nearby late-type galaxies (Pilyugin et al. 2014a,b).

We constructed radial surface-brightness profiles of our galaxies in the infrared $W1$ band using the photometric maps obtained by the *WISE* satellite (Wright et al. 2010). The characteristics of the disk for each galaxy were obtained through bulge-disk decomposition. The radial distributions of the oxygen abundances predicted by the parametric OH – SB relation are compared to the radial distributions of the oxygen abundances determined from the analysis of the emission-line spectra of the H II regions in our target galaxies.

The paper is organized as follows. Our sample of galaxies is presented in Section 2. The spectroscopic observations and data reduction are described in Section 3. The photometric properties of our galaxies are discussed in Section 4. The oxygen abundances are presented in Section 5. Section 6 contains a discussion and a brief summary of the main results.

Throughout the paper, we will use the following standard notations for the line intensities I :

$$\begin{aligned} R &= I_{[\text{O III}]\lambda 4363} / I_{\text{H}\beta}, \\ R_2 &= I_{[\text{O II}]\lambda 3727 + \lambda 3729} / I_{\text{H}\beta}, \\ N_2 &= I_{[\text{N II}]\lambda 6548 + \lambda 6584} / I_{\text{H}\beta}, \\ S_2 &= I_{[\text{S II}]\lambda 6717 + \lambda 6731} / I_{\text{H}\beta}, \\ R_3 &= I_{[\text{O III}]\lambda 4959 + \lambda 5007} / I_{\text{H}\beta}. \end{aligned}$$

2. Our galaxy sample

Our original sample of spiral galaxies for follow-up observations with the Southern African Large Telescope (SALT; Buckley et al. 2006; O’Donoghue et al. 2006) was devised based on Sloan Digital Sky Survey (SDSS) images and the fact that SALT can observe targets with a declination $\delta < 10$ degrees and has a field of view of 8 arcmin. Each selected spiral galaxy contains a sufficiently large number of bright H II regions distributed across the whole galaxy disk and fitting SALT’s field of view. The total sample consists of ~ 30 nearby galaxies that are located in the equatorial sky region.

Out of this sample of 58 galaxies, we have obtained spectra of H II regions in six galaxies (NGC 1087, NGC 2967, NGC 3023, NGC 4030, NGC 4123, NGC 4517A) thus far. In Fig. 1 we present the images and slit positions for those galaxies. For a detailed description of the observations we refer to Section 3.

Table 1 lists the general characteristics of each galaxy. We listed the most widely used identifications for our target galaxies, i.e., the designations in the New General Catalogue (NGC) and in the Uppsala General Catalog of Galaxies (UGC). The morphological type of the galaxy and morphological type code T were adopted from LEDA (Lyon-Meudon Extragalactic Database; Paturel et al. 1989, 2003). The right ascension and declination were taken from the NASA/IPAC Extragalactic Database (NED)¹. The inclination of each galaxy, the position

angle of the major axis, and the isophotal radius R_{25} in arcmin of each galaxy were determined in our current study. The distances were taken from NED. These distances include flow corrections for the Virgo cluster, the Great Attractor, and Shapley Supercluster infall. The isophotal radius in kpc was estimated from the isophotal radius R_{25} in arcmin and the distance listed above. The characteristics of the disks (the surface brightness at the disk center in the $W1$ band and the disk scale length) were determined through the bulge-disk decomposition carried out in our current paper. The surface brightness at the disk center was reduced to a face-on galaxy orientation and is given in terms of $L_{\odot} \text{pc}^{-2}$.

Three galaxies of our sample are members of pairs of galaxies and are included in the “Catalogue of Isolated Pairs of Galaxies in the Northern Hemisphere” (Karachentsev 1972): NGC 3023 = KPG 216B, NGC 4123 = KPG 322B, NGC 4517A = KPG 344A. Two galaxies of our sample, NGC 2967 and NGC 4030, are known members of galaxy groups (Fouqué et al. 1992; Garcia 1993). The galaxy NGC 4517A is a low-surface-brightness galaxy (Romanishin et al. 1983).

3. Spectroscopic observations and reduction

3.1. Observing procedures

The spectroscopic observations of our selected galaxies were obtained with the multi-object spectroscopic mode (MOS) of the Robert Stobie Spectrograph (RSS; Burgh et al. 2003; Kobulnicky et al. 2003) installed at SALT. For each galaxy from our sample we constructed a MOS mask, where the slit positions for the H II regions were selected using *gri* SDSS images. A typical MOS mask thus devised contained 9–12 slits for H II regions distributed over the whole galaxy disk. The usual width of the slits was 1.5 arcsec. The general strategy of the observations was to cover the total spectral range of 3600–7000 Å in order to detect (1) the Balmer lines $H\delta$, $H\gamma$, $H\beta$ and $H\alpha$, which were used for extinction corrections, and (2) various emission lines used for the calculation of abundances: $[\text{O II}]\lambda 3727, 3729$, $[\text{O III}]\lambda 4363$, $[\text{O III}]\lambda 4959, 5007$, $[\text{N II}]\lambda 6548, 6584$ and $[\text{S II}]\lambda 6717, 6731$. We chose a resolution of $R = 1000$ – 2000 in order to be able to resolve emission lines located close to each other, e.g., $H\gamma$ and $[\text{O III}]\lambda 4363$, or $[\text{S II}]\lambda 6717$ and $[\text{S II}]\lambda 6731$.

In MOS mode the actual spectral coverage for each slit varies slightly depending on the X-position of a given slit relative to the center of the mask. Thus, to cover the total desired spectral range of 3600–7000 Å for each slit of the mask we had to obtain two spectral setups for each studied galaxy: One ranging from 3500–6500 Å (referred to as the blue setup hereafter) and one from 5000–7000 Å (called the red setup hereafter), and to combine them after data reduction.

The volume phase holographic (VPH) grating GR900 was used to cover the blue setup with a final reciprocal dispersion of $\sim 0.97 \text{ \AA pixel}^{-1}$ and a spectral resolution resulting in a FWHM of 5–6 Å ($R \sim 1000$). In order to cover the red setup, we used the VPH grating GR1300 with a final reciprocal dispersion of $\sim 0.64 \text{ \AA pixel}^{-1}$ and a spectral resolution with a FWHM of 3–4 Å ($R \sim 1600$). All observations were carried out between June 2012 and April 2013.

SALT is a telescope where during an observation the mirror remains at a fixed altitude and azimuth and the image of an astronomical target produced by the telescope is followed by the “tracker”, which is located at the position of the prime focus (similar in operation to the Arecibo Radio Telescope). This results in only a limited observing window per target. For this

¹ The NASA/IPAC Extragalactic Database (NED) is operated by the Jet Propulsion Laboratory, California Institute of Technology, under contract with the National Aeronautics and Space Administration. <http://ned.ipac.caltech.edu/>

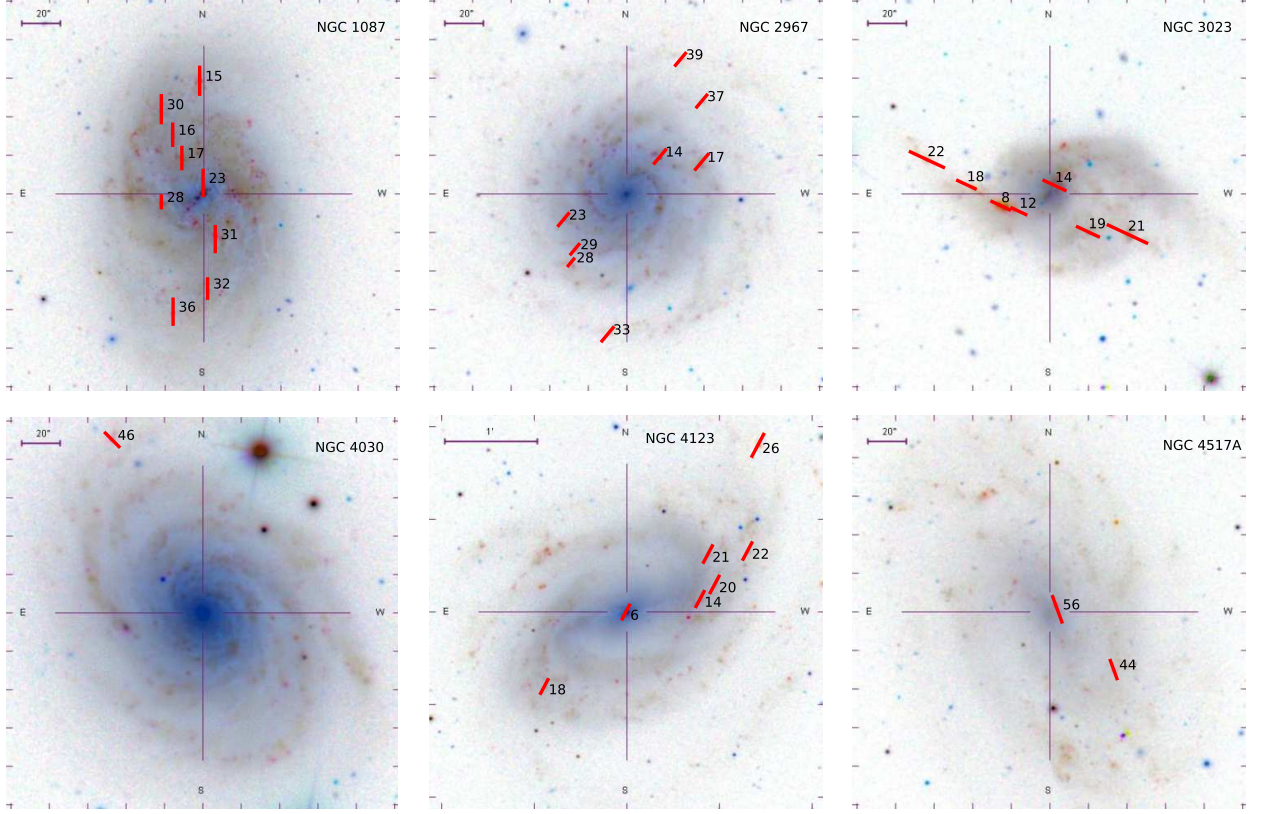


Fig. 1. SDSS images of our target galaxies with marked positions of the slits used in the present investigation.

Table 1. The adopted and derived properties of our target galaxies

Name	NGC 1087	NGC 2967	NGC 3023	NGC 4030	NGC 4123	NGC 4517A
	UGC 2245	UGC 5180	UGC 5269	UGC 6993	UGC 7116	UGC 7685
Morphological type, type code T	SABc, 5.0	Sc, 5.2	SABc, 5.5	Sbc, 4.0	Sc, 5.0	SBdm, 8.0
Right ascension (J2000.0) [deg]	41.604852	145.513729	147.469112	180.098445	182.046296	188.117319
Declination (J2000.0) [deg]	-0.498649	0.336438	0.618167	-1.100095	2.878283	0.389670
Inclination [deg], ellipticity	53.0, 0.39	21.6, 0.07	49.5, 0.35	36.9, 0.20	43.1, 0.27	50.2, 0.36
Position angle [deg]	1	151	86	38	128	23
Isophotal radius R_{25}^a [arcmin]	1.86	1.33	1.02	1.89	1.69	1.40
Distance [Mpc]	20.1	29.5	29.4	26.4	27.3	27.8
Isophotal radius R_{25} [kpc]	10.86	11.41	8.72	14.51	13.42	11.32
Disk scale length in $W1$ band [kpc]	2.45	1.97		3.36	4.70	4.90
Logarithm of $W1$ brightness of disk center ^b [$L_{\odot} \text{pc}^{-2}$]	3.056	3.315		3.234	2.557	1.955

^a in the B band

^b reduced to a face-on galaxy orientation

reason each observation consisted usually of two exposures of about 1000 s each to fit a single SALT visibility track. For the same reason the blue and red setups were usually observed in different nights.

Spectra of Ar comparison arcs and a set of quartz tungsten halogen flats were obtained immediately after each observation to calibrate the wavelength scale and to correct for pixel-to-pixel variations. A set of spectrophotometric standard stars was observed during twilight time for the relative flux calibration. Since SALT has a variable pupil size, an absolute flux calibration is not possible even using spectrophotometric standard stars. All

details of the observations are summarized in Table 2. In total, 34 H II regions in six galaxies were observed.

The primary reduction of the SALT data was done with the SALT science pipeline (Crawford et al. 2010). After that, the bias- and gain-corrected and mosaiced MOS data were reduced in the way described below.

Table 2. Journal of the observations.

Galaxy	Date for blue setup	Date for red setup	Exposure time for blue setup	Exposure time for red setup	Seeing for blue setup	Seeing for red setup
NGC 1087	...	2012.12.20	...	2×1000	...	1.4''
NGC 2967	2013.02.02	2013.02.02	2×1000	2×1000	1.5''	1.2''
NGC 3023	2013.01.05	2013.01.06	2×1000	2×1000	2.5''	2.3''
NGC 4030	2013.03.20	...	2×1000	...	1.0''	...
NGC 4123	2013.04.29	2013.03.03	2×1000	2×910	1.7''	2.2''
NGC 4517A	2012.06.16	...	1×900+2×725	...	1.7''	...

3.2. Data reduction and line flux measurements

Cosmic ray rejection was done using the IRAF² task `lacospec` (van Dokkum 2001). The wavelength calibration was accomplished using the IRAF tasks `identify`, `reidentify`, `fitcoord`, and `transform`. The spectral data were divided by the illumination-corrected flat field in order to correct for pixel-to-pixel sensitivity variations of the detector. After that two-dimensional spectra were extracted from the MOS images for each slit. The background subtraction was done using the IRAF task `background`. Since we used a multi-slit mask, the slits for the individual objects have a length of $\sim 5 - 20$ arcsec and the background was fitted by a low-order polynomial function along the spatial slit coordinate at each wavelength. This allows us to extract the flux from the H II regions only, without galactic stellar background. The spectra were corrected for sensitivity effects using the Sutherland extinction curve and a sensitivity curve obtained from observed standard star spectra. Finally, all two-dimensional spectra of a slit position obtained with the same observational setup were averaged.

From each two-dimensional spectrum of the blue and red setups, one-dimensional spectra were extracted in spatial direction for each pixel along the slit. We refer to these spectra as “one-pixel-wide”. The line fluxes ([O II] $\lambda\lambda$ 3727,3729, [O III] λ 4363, H β , [O III] λ 4959, [O III] λ 5007, [N II] λ 6548, H α , [N II] λ 6584, [S II] λ 6717, and [S II] λ 6731) were then measured with IRAF or/and by fitting the lines with Gaussians following Pilyugin & Thuan (2007) and Pilyugin et al. (2010a).

We first consider the distribution of the emission-line fluxes along the slit. The measured fluxes in the H β and R_3 emission lines in the blue and red one-pixel-wide spectra for slit 8 in NGC 3023 as a function of the pixel number along the slit are shown in Fig. 2. Examination of Fig. 2 shows that the position of the peak in the H β (and R_3) emission line in the red spectrum is shifted as compared to that in the blue spectrum by approximately three pixels. This shows that the position of the slit of the red spectrum does not coincide with the position of the slit for the blue spectrum. Instead they are shifted in the direction along the slit by approximately three pixels with respect to each other. Inspection of Fig. 2 also shows that the form of the distribution of the H β (and R_3) emission-line flux per pixel in the red spectrum differs from that in the blue spectrum. This demonstrates that the position of the slit for the red spectrum is also shifted in the direction perpendicular to the slit or that the position angles of the red and blue spectrum are different. This prevents us from considering the lines of the blue and red spectra together. Therefore we derived the abundances using the lines from the blue (or red) spectrum individually.

The full set of lines [O II] $\lambda\lambda$ 3727,3729, H β , [O III] λ 5007, H α , and [N II] λ 6548 or H β , [O III] λ 5007, H α , [N II] λ 6584 and [S II] $\lambda\lambda$ 6717,6731 is needed to correct for interstellar reddening and to determine the oxygen abundances. For this reason only slits that provide at least one of these line sets in either the blue or red setup are chosen for further study. As the actual spectral coverage for each of our slits varies slightly depending on the position of a given slit on the mask, in some cases the H β + [O III] λ 5007 lines of the red spectra and the H α + [N II] λ 6548 lines of the blue spectra are shifted beyond the actual spectral coverage of the slit. This is the reason why the number of the presented observations of H II regions varies from one in NGC 4030 to up to 9 in NGC 1087.

We constructed the aperture for the blue and red spectra by averaging the seven one-pixel-wide spectra near the flux maximum. As mentioned before, the emission from the underlying stellar population of the galactic disk was subtracted during the background correction, i.e., we removed the stellar continuum averaged along the spatial slit coordinates near the H II region. Since the continuum in the spectra of our H II regions is sufficiently weak or undetectable, we neglected possible stellar absorption by the stellar populations of the H II regions. The measured emission fluxes F were corrected for interstellar reddening. We obtained the extinction coefficient $C(\text{H}\beta)$ using the theoretical H α -to-H β ratio (= 2.878) and the analytical approximation to the Whitford interstellar reddening law of Izotov et al. (1994).

The dereddened emission-line fluxes in the averaged spectra of the target H II regions are listed in Table 3 for the blue spectra and in Table 4 for the red spectra. The theoretical ratio of [N II] λ 6584/[N II] λ 6548 is constant and close to 3 (Storey & Zeippen 2000) since those lines originate from transitions from the same energy level. Since the [N II] λ 6584 line measurements are more reliable than the [N II] λ 6548 line measurements the value of N_2 is estimated as $N_2 = 1.33 \times [\text{N II}]\lambda 6584$ unless indicated otherwise. Similarly, the value of R_3 can be estimated as $R_3 = 1.33 \times [\text{O III}]\lambda 5007$ since the [O III] λ 5007 and [O III] λ 4959 lines originate also from transitions from the same energy level and their flux ratio is very close to 3 (Storey & Zeippen 2000; Kniazev et al. 2004). Therefore, the [N II] λ 6548 and λ 4959 lines are not included in Table 3 and Table 4.

The uncertainty of the emission-line flux ε_{line} is estimated taking into account the uncertainty of the continuum level, errors in the line flux and the uncertainty in the sensitivity curve (see Kniazev et al. 2004, for details). The uncertainty of the continuum, ε_{cont} , is determined in the region near the emission line where the continuum is approximated by a linear fit. The line-flux uncertainty, ε_{flux} , is estimated as the deviation from a Gaussian profile. The uncertainty in the sensitivity curve, ε_{sc} , is less than 2 – 3% in all considered wavelength ranges (see, e.g., Kniazev 2012). We adopt the maximum value of the relative uncertainty $\varepsilon_{sc} = 0.03$.

² IRAF is distributed by the National Optical Astronomical Observatories, which are operated by the Association of Universities for Research in Astronomy, Inc., under cooperative agreement with the National Science Foundation.

Table 3. The dereddened emission line fluxes (in units of the $H\beta$ line flux) and the extinction coefficient $C(H\beta)$ in the blue spectra of a sample of the target H II regions in NGC 3023.

Slit	R.A. ^a	DEC. ^a	[O II] λ 3727,3729	[O III] λ 4363	[O III] λ 5007	[N II] λ 6584	[S II] λ 6717	[S II] λ 6731	$C(H\beta)$
NGC 2967									
17	145.503249	0.340438	2.712 ± 0.164		0.371 ± 0.033	0.772 ± 0.044			0.579
33	145.516052	0.316465	4.603 ± 0.662		1.788 ± 0.180	0.621 ± 0.041			0.704
NGC 3023									
8	147.476616	0.616676	1.627 ± 0.051	0.072 ± 0.003	6.117 ± 0.200				0.297
12	147.474086	0.615905	2.600 ± 0.084	0.030 ± 0.003	3.280 ± 0.109				0.317
14	147.468182	0.619303	3.662 ± 0.120		1.654 ± 0.057	0.474 ± 0.021			0.345
NGC 4030									
46	180.111544	-1.074890	2.340 ± 0.104		0.820 ± 0.034	0.849 ± 0.038			0.524
NGC 4123									
14	182.032991	2.880344	2.281 ± 0.131		0.457 ± 0.031	0.858 ± 0.036			0.535
20	182.030381	2.882922	2.324 ± 0.139		0.896 ± 0.045	0.817 ± 0.039			0.403
21	182.031526	2.888546	2.322 ± 0.146		0.473 ± 0.036	0.903 ± 0.040			0.689
22	182.024433	2.888972	2.925 ± 0.166		0.781 ± 0.051	0.694 ± 0.032	0.483 ± 0.026	0.331 ± 0.017	0.485
26	182.022560	2.908112	1.771 ± 0.088		3.457 ± 0.142	0.217 ± 0.014			0.113
NGC 4517A									
44	188.108016	0.381373	4.566 ± 0.224		0.936 ± 0.050	0.269 ± 0.020			0.402
56	188.116422	0.390758	2.310 ± 0.084		2.109 ± 0.096	0.305 ± 0.021			0.194

^a in degrees (J2000).**Table 4.** The dereddened emission line fluxes (in units of the $H\beta$ line flux) and the extinction coefficient $C(H\beta)$ in the red spectra of a sample of the target H II regions in our galaxy sample.

Slit	R.A. ^a	DEC. ^a	[O III] λ 5007	[N II] λ 6584	[S II] λ 6717	[S II] λ 6731	$C(H\beta)$
NGC 1087							
15	41.605348	-0.482317	0.794 ± 0.034	0.633 ± 0.030	0.410 ± 0.018	0.292 ± 0.013	0.353
16	41.609253	-0.490142	0.494 ± 0.020	0.750 ± 0.029	0.479 ± 0.017	0.336 ± 0.013	0.282
17	41.607925	-0.493503	0.400 ± 0.031	0.664 ± 0.026	0.377 ± 0.018	0.259 ± 0.014	0.306
23	41.604852	-0.497109	0.211 ± 0.011	0.935 ± 0.043	0.373 ± 0.017	0.278 ± 0.012	0.380
28	41.610902	-0.500035	0.429 ± 0.033	0.754 ± 0.026	0.443 ± 0.020	0.334 ± 0.015	0.252
30	41.610902	-0.486017	0.427 ± 0.017	0.696 ± 0.033	0.320 ± 0.016	0.225 ± 0.010	0.340
31	41.603092	-0.504827	0.449 ± 0.014	0.764 ± 0.027	0.275 ± 0.009	0.206 ± 0.007	0.443
32	41.604192	-0.512645	0.932 ± 0.036	0.615 ± 0.031	0.464 ± 0.027	0.322 ± 0.023	0.417
36	41.609197	-0.515824	0.406 ± 0.021	0.589 ± 0.025	0.402 ± 0.016	0.280 ± 0.016	0.251
NGC 2967							
14	145.509118	0.341424	0.129 ± 0.013	0.840 ± 0.031	0.309 ± 0.013	0.226 ± 0.009	0.900
23	145.522704	0.332752	0.195 ± 0.060	0.820 ± 0.046	0.395 ± 0.024	0.270 ± 0.019	1.040
28	145.521731	0.326422	0.930 ± 0.048	0.613 ± 0.045	0.328 ± 0.031	0.216 ± 0.019	0.970
29	145.520986	0.328543	0.294 ± 0.070	0.676 ± 0.031	0.350 ± 0.029	0.252 ± 0.035	0.734
37	145.502932	0.349615	0.738 ± 0.126	0.689 ± 0.061	0.608 ± 0.049	0.295 ± 0.050	0.902
39	145.505741	0.355989	1.596 ± 0.199	0.530 ± 0.059	0.451 ± 0.064	0.229 ± 0.055	0.644
NGC 3023							
8	147.476616	0.616676	5.680 ± 0.204	0.092 ± 0.004	0.122 ± 0.005	0.089 ± 0.004	0.255
12	147.474086	0.615905	3.118 ± 0.103	0.221 ± 0.008	0.225 ± 0.009	0.165 ± 0.007	0.181
14	147.468182	0.619303	1.740 ± 0.064	0.414 ± 0.017	0.456 ± 0.019	0.332 ± 0.016	0.222
18	147.480337	0.619130	3.482 ± 0.130	0.147 ± 0.006	0.225 ± 0.010	0.146 ± 0.006	0.058
19	147.463502	0.612667	2.479 ± 0.110	0.429 ± 0.041	0.500 ± 0.044	0.434 ± 0.044	0.541
21	147.457781	0.612337	1.872 ± 0.071	0.309 ± 0.016	0.484 ± 0.021	0.337 ± 0.016	0.104
22	147.486919	0.623162	2.748 ± 0.094	0.136 ± 0.009	0.240 ± 0.011	0.167 ± 0.009	0.078
NGC 4123							
6	182.046371	2.878087	0.267 ± 0.012	1.523 ± 0.051	0.334 ± 0.011	0.363 ± 0.012	1.086
18	182.061021	2.864815	0.455 ± 0.043	0.816 ± 0.039	0.584 ± 0.033	0.478 ± 0.035	0.424

^a in degrees (J2000).

4. Photometry

To estimate the deprojected galactocentric distance (normalized to the optical isophotal radius R_{25}) of the H II region from its coordinates on the celestial sphere one needs to know the values of the inclination, i , the position angle of the major axis, PA , and the isophotal radius of a galaxy, R_{25} . It is common practice

to take those values from de Vaucouleurs et al. (1991, thereafter RC3) or from the LEDA database. However, some values from those sources show a significant difference for galaxies from our list. For example, the isophotal radius of NGC 4517A in the RC3 is larger by a factor of two than that given in the LEDA database.

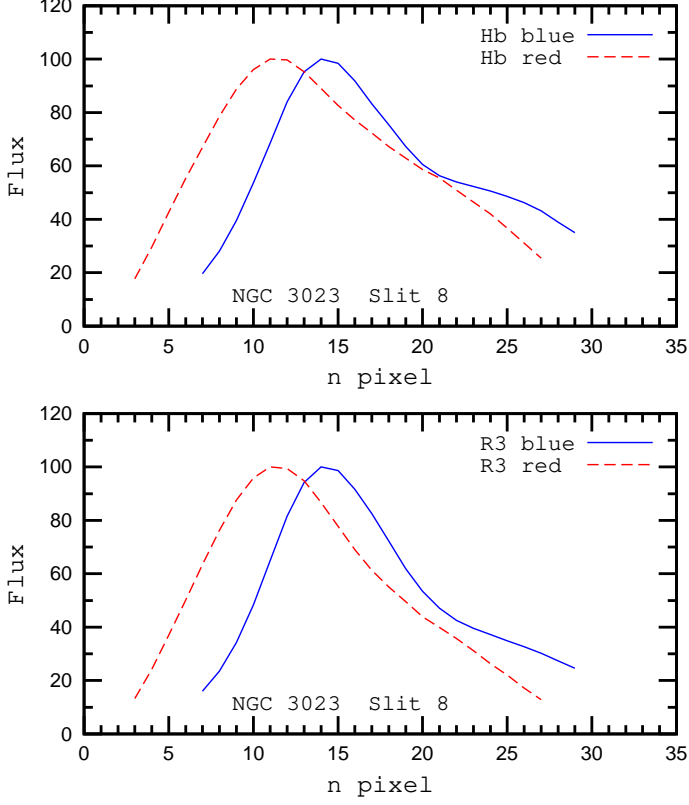


Fig. 2. The fluxes in the $H\beta$ (upper panel) and R_3 (lower panel) emission lines in the blue (solid lines) and red (dashed lines) spectra as a function of the pixel number along the slit for slit 8 in NGC 3023. The fluxes are in arbitrary units.

Therefore we obtained our own estimates of the values of i , PA , and R_{25} for our target galaxies.

We analyzed the publicly available photometric maps in the infrared $W1$ band (with an isophotal wavelength of $3.4 \mu\text{m}$) obtained by the *Wide-field Infrared Survey Explorer* (*WISE*) (Wright et al. 2010) and in the g and r bands obtained by the *Sloan Digital Sky Survey* (*SDSS*; data release 9 (DR9), Ahn et al. 2012). We derived the surface-brightness profile and disk orientation parameters in three photometric bands for each galaxy. The determinations of the surface-brightness profile, position angle, and ellipticity were performed for each band separately in the way described in Pilyugin et al. (2014b). But for NGC 3023 we were not able to estimate reliable values of the position angle and ellipticity for the g and r bands. Therefore, for this galaxy the values of the position angle and ellipticity obtained for the $W1$ band were used for the construction of the surface-brightness profiles in all three filters.

It should be noted that the *WISE* and *SDSS* surveys are sufficiently deep for our surface-brightness profiles to extend beyond the optical isophotal radii R_{25} . The obtained surface-brightness profiles are shown in Fig. 3. The adopted inclinations and position angles are given in Table 1.

The value of the isophotal radius is derived from the obtained surface-brightness profiles in the g and r bands. Surface-brightness measurements were corrected for foreground Galactic extinction using the A_V values from the recalibration by Schlafly & Finkbeiner (2011) of the extinction maps of Schlegel et al. (1998) and the extinction curve of Cardelli et al. (1989), assuming a ratio of total to selective extinction of $R_V = A_V/E_{B-V} = 3.1$. The A_V values given in the NASA

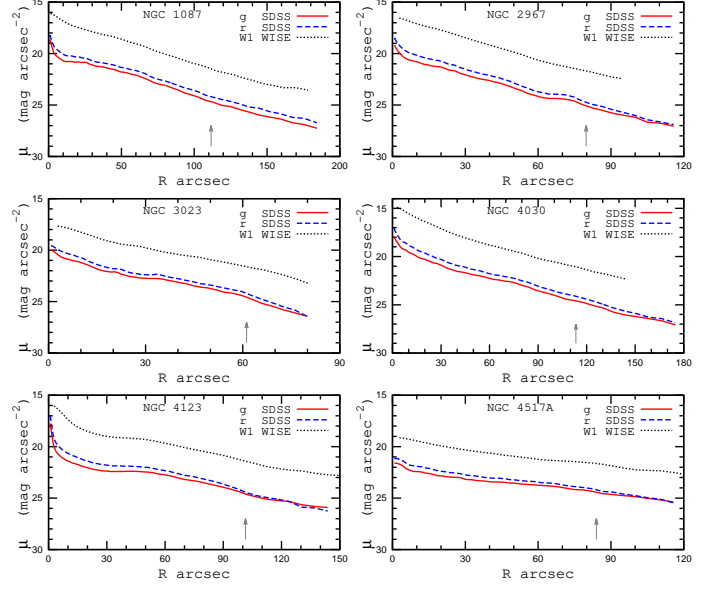


Fig. 3. The observed surface-brightness profiles of our galaxies in the g and r bands of the *SDSS* photometric system and in the $W1$ band of the *WISE* photometric system. The X-axis shows the galactocentric radius in arcsec, and the Y-axis the surface brightness in mag arcsec^{-2} . The optical isophotal radius R_{25} is marked by an arrow.

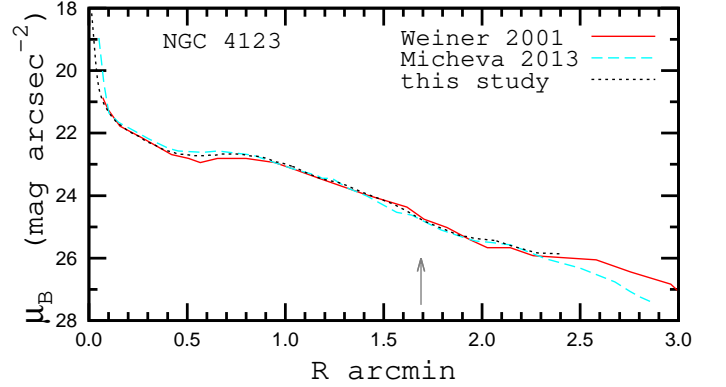


Fig. 4. Comparison between the measured surface-brightness profiles of NGC 4123 in the B band reported by Weiner et al. (2001) (solid line), by Micheva et al. (2013) (long-dashed line), and obtained here (short-dashed line). The X-axis shows the galactocentric radius in arcmin, and the Y-axis the surface brightness in mag arcsec^{-2} . The arrow indicates the optical isophotal radius R_{25} .

Extragalactic Database NED were used. Afterwards the surface-brightness measurements were corrected for the inclination. The measurements in the *SDSS* filters g and r were converted to B -band magnitudes, and the AB magnitudes were reduced to the Vega photometric system using the conversion relations and solar magnitudes of Blanton & Roweis (2007). First, the B -band magnitudes were obtained from the g and r magnitudes

$$B_{AB} = g + 0.2354 + 0.3915 [(g - r) - 0.6102], \quad (1)$$

where the B_{AB} , g , and r magnitudes in Eq. (1) are in the AB photometric system. Then, the AB magnitudes were reduced to the Vega photometric system

$$B_{Vega} = B_{AB} + 0.09. \quad (2)$$

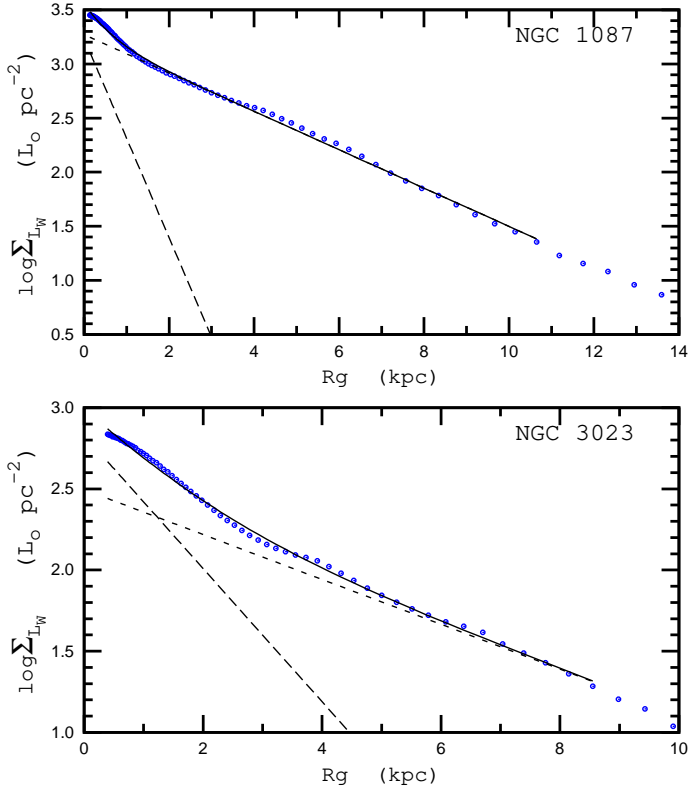


Fig. 5. The patterns resulting from the bulge-disk decomposition of our target galaxies (X-axis: galactocentric radius in kpc, Y-axis: logarithm of the central surface brightness for a face-on galaxy orientation in solar luminosities per pc²). Each panel shows the decomposition assuming a purely exponential profile for the disk. The measured surface profile is plotted using gray (blue) circles. The bulge contribution is shown by a dotted line, the disk contribution by a dashed line, and the total (bulge + disk) fit by a solid line.

The obtained isophotal radii are given in Table 1.

Surface brightness profiles of the galaxy NGC 4123 in the *B* band were published by Weiner et al. (2001) and Micheva et al. (2013). Fig. 4 shows the comparison between their profiles with the one derived here from the photometric imaging data in the *SDSS g* and *r* bands.

We performed a bulge-disk decomposition of the observed surface-brightness profiles using a purely exponential disk (PED) approximation in the same way as in Pilyugin et al. (2014b). Exponential profiles were used to fit the observed disk surface-brightness profiles, and the bulge profiles were fitted with a general Sérsic profile. The observed surface-brightness profiles of five galaxies from our sample are fitted satisfactorily well. The upper panel of Figure 5 shows the bulge-disk decomposition of the galaxy NGC 1087 as an example. The measured surface profile is marked by circles. The fit to the bulge contribution is shown by a dotted line, the fit to the disk by a dashed line, and the total (bulge + disk) fitting by a solid line. Table 1 lists the parameters of the disk surface-brightness profiles of those galaxies in the *W1* band: the logarithm of the central surface brightness of the disk in the *W1* band reduced to a face-on galaxy orientation in terms of $L_{\odot} \text{ pc}^{-2}$ and the disk scale length in the *W1* band, h_{W1} in kpc. Those values are parameters of the exponential disk approximation, described in detail in Pilyugin et al. (2014b).

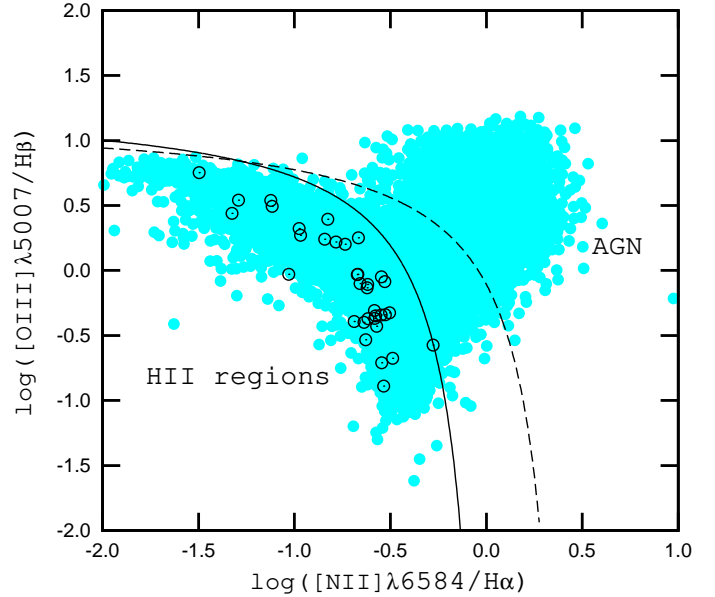


Fig. 6. The $[\text{N II}]\lambda 6584/\text{H}\alpha$ versus $[\text{O III}]\lambda 5007/\text{H}\beta$ diagram. The symbols denote results for the measured H II regions in our target galaxies. The solid line separates objects with H II region spectra from those containing an AGN according to Kauffmann et al. (2003), while the dashed line represents the same separation according to the work by Kewley et al. (2001). The gray (light-blue) filled circles show a large sample of emission-line *SDSS* galaxies from Thuan et al. (2010).

For the galaxy NGC 3023, we could not determine a reliable disk scale length, h_{W1} , and central surface brightness of the disk, $(\Sigma_{L_{W1}})_0$. The lower panel of Figure 5 shows the surface-brightness-profile fit for this galaxy. The disk contribution to the surface brightness is close to the observed surface-brightness profile over a small interval of radial distances only (in fact, this is a bulge-dominated galaxy). Therefore, the values of the disk scale length and central surface brightness of the disk are questionable.

5. Abundances

5.1. Abundance determination

Baldwin et al. (1981) proposed the $[\text{O III}]\lambda 5007/\text{H}\beta$ vs. $[\text{N II}]\lambda 6584/\text{H}\alpha$ diagram (the so-called BPT classification diagram) which is often used to distinguish between star-forming regions and AGNs. The exact location of the dividing line between star-forming regions and AGNs is still controversial (see, e.g., Kewley et al. 2001; Kauffmann et al. 2003). Fig. 6 shows the positions of our targets (open circles) in the BPT classification diagram. The solid line is the dividing line between star-forming regions and AGNs according to Kauffmann et al. (2003), while the dashed line is the same line according to Kewley et al. (2001). Regardless of which line is adopted, Fig. 6 shows that all our objects are H II regions and their oxygen abundances can be estimated using standard techniques.

The T_e -based oxygen $(\text{O}/\text{H})_{T_e}$ abundances of the H II regions with the detected auroral line $[\text{O III}]\lambda 4363$ were determined using the equations for the T_e -method from Pilyugin et al. (2010b, 2012).

A new method (called the “*C* method”) for oxygen and nitrogen abundance determinations from strong emission lines was

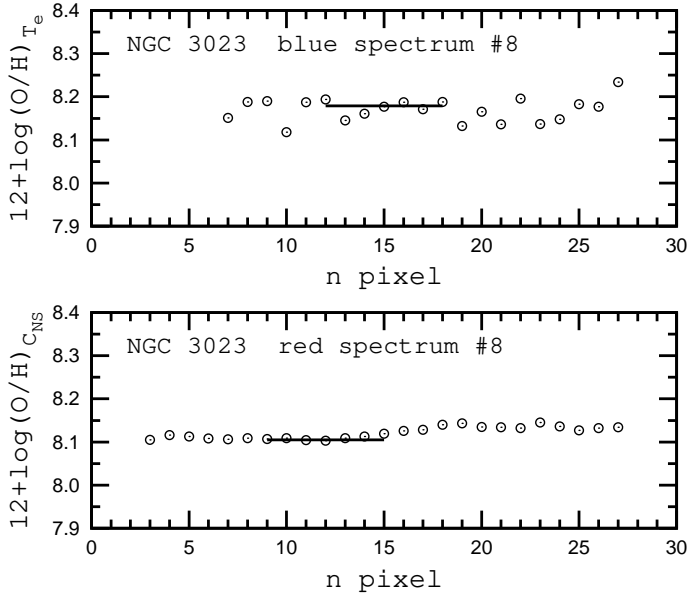


Fig. 7. The oxygen abundances as a function of the number of the pixel along the slit for the slit 8 in the NGC 3023. The circles in the upper panel show the oxygen abundances determined from the individual blue one-pixel-width spectra through the T_e method. The solid line is the abundance obtained from the integrated seven-pixel-width spectrum through the T_e method. The circles in the lower panel show the oxygen abundances determined from the individual red one-pixel-width spectra through the C_{NS} method. The solid line is the abundance obtained from the integrated seven-pixel-width spectrum through the C_{NS} method.

recently suggested (Pilyugin et al. 2012, 2014a). In our red spectra, we measured the strong lines R_3 , N_2 , and S_2 , which allowed us to determine the oxygen $(O/H)_{C_{NS}}$ abundances using those strong lines. In some of our blue spectra, the strong lines R_2 , R_3 , and N_2 were measured and applied to determine the oxygen $(O/H)_{C_{ON}}$ abundances.

5.2. The robustness and precision of the abundance determination

The emission-line fluxes measured in the one-pixel-wide spectra represent the radiation of a small part of the H II region. One would expect that the T_e -based abundances in a given H II region derived from the spectra of different areas on the H II region image should be the same or at least should be close to each other. Is this the case for the abundances estimated from the counterpart method? To clarify this matter we have estimated the oxygen abundances from the individual one-pixel-wide spectra and considered the variations in those abundances.

Fig. 7 shows the distribution of the oxygen abundances along the slit for the bright, extend H II region (# 8) in NGC 3023, i.e., the abundance estimated from the individual one-pixel-wide spectra as a function of the number of the pixel along the slit. The auroral line $R = [O III]\lambda 4363$ is detected in around 20 individual one-pixel-wide spectra of this H II region. The circles in the upper panel of the Fig. 7 show the oxygen abundances determined from the individual blue one-pixel-wide spectra through the T_e method. The solid line is the T_e -based abundance obtained from the seven-pixel-wide spectrum. The circles in the lower panel of the Fig. 7 show the oxygen abundances determined from the

individual red one-pixel-wide spectra through the C_{NS} method. The solid line represents the abundance obtained from the seven-pixel-wide spectrum through the C_{NS} method.

Inspection of the upper panel of Fig. 7 confirms that the T_e -based abundances are independent from the position in the H II region image at which the measurement was taken. Examination of the lower panel of Fig. 7 shows that the abundances determined from the individual one-pixel-wide spectra through the C method are close to each other and are close to the abundance obtained from the integrated seven-pixel-wide spectrum. A similar picture was found for other H II regions. Thus, the C -based abundances are robust and independent from the specific area covered by the measurement in an H II region image, i.e., the C method produces a reliable oxygen abundance even if a spectrum of only part of an H II region is used.

The scatter in individual C -based abundances is even lower than the scatter in individual T_e -based abundances, i.e., the formal uncertainty in the C -based abundances is lower than that in the T_e -based abundances. This can be attributed to the fact that the measurements of the weak auroral lines used in the T_e method can involve larger errors than the measurements of the strong lines used in the C method. It should be noted, however, that the true uncertainty in the C -based oxygen abundance does not only depend on the accuracy of the strong-line measurements in the spectrum of the target H II region but also on the reliability of the abundance determinations in the reference H II regions. Our current sample of reference H II regions (our standard reference sample from 2013) contains 250 H II regions for which the absolute differences in the oxygen abundances $(O/H)_{C_{ON}} - (O/H)_{T_e}$ and $(O/H)_{C_{NS}} - (O/H)_{T_e}$ and in the nitrogen abundances $(N/H)_{C_{ON}} - (N/H)_{T_e}$ and $(N/H)_{C_{NS}} - (N/H)_{T_e}$ are less than 0.1 dex (Pilyugin et al. 2014a). Thus the true uncertainty in the C -based oxygen abundance may be up to around 0.1 dex even if the formal error due to the uncertainties in the strong-line measurement is small. Therefore we assume that the uncertainties in the obtained oxygen abundances in our investigated H II regions in the current paper can exceed 0.1 dex although the formal error caused by the uncertainty in the line fluxes measurement is lower.

5.3. Radial gradients

The radial distribution of the oxygen abundances across the disk within the isophotal radius in each of our target galaxies was fitted with the following equation:

$$12 + \log(O/H) = 12 + \log(O/H)_{R_0} + C_{O/H} \times (R/R_{25}), \quad (3)$$

where $12 + \log(O/H)_{R_0}$ is the oxygen abundance at $R_0 = 0$, i.e., the extrapolated central oxygen abundance, $C_{O/H}$, is the slope of the oxygen abundance gradient expressed in terms of dex R_{25}^{-1} , and R/R_{25} is the fractional radius (the galactocentric distance normalized to the disk's isophotal radius R_{25}).

NGC 1087. The strong lines $H\beta$, $[O III]\lambda\lambda 4959, 5007$, $H\alpha$, $[N II]\lambda\lambda 6548, 6584$, and $[S II]\lambda\lambda 6717, 6731$ were measured in nine red spectra. In those H II regions, we derived the oxygen abundance $(O/H)_{C_{NS}}$. The resulting oxygen abundances are listed in Table 5. Those abundances are shown by the filled circles in panel *a* of Fig. 8.

There are three *SDSS* spectra of H II regions in the galaxy NGC 1087 in data release 7 (DR7, Abazajian et al. 2009), namely Sp 409-51871-237, Sp 1069-52590-193, and Sp 1511-52946-192. (The *SDSS* spectrum number consists of the *SDSS* plate number, the modified Julian date of the observation, and

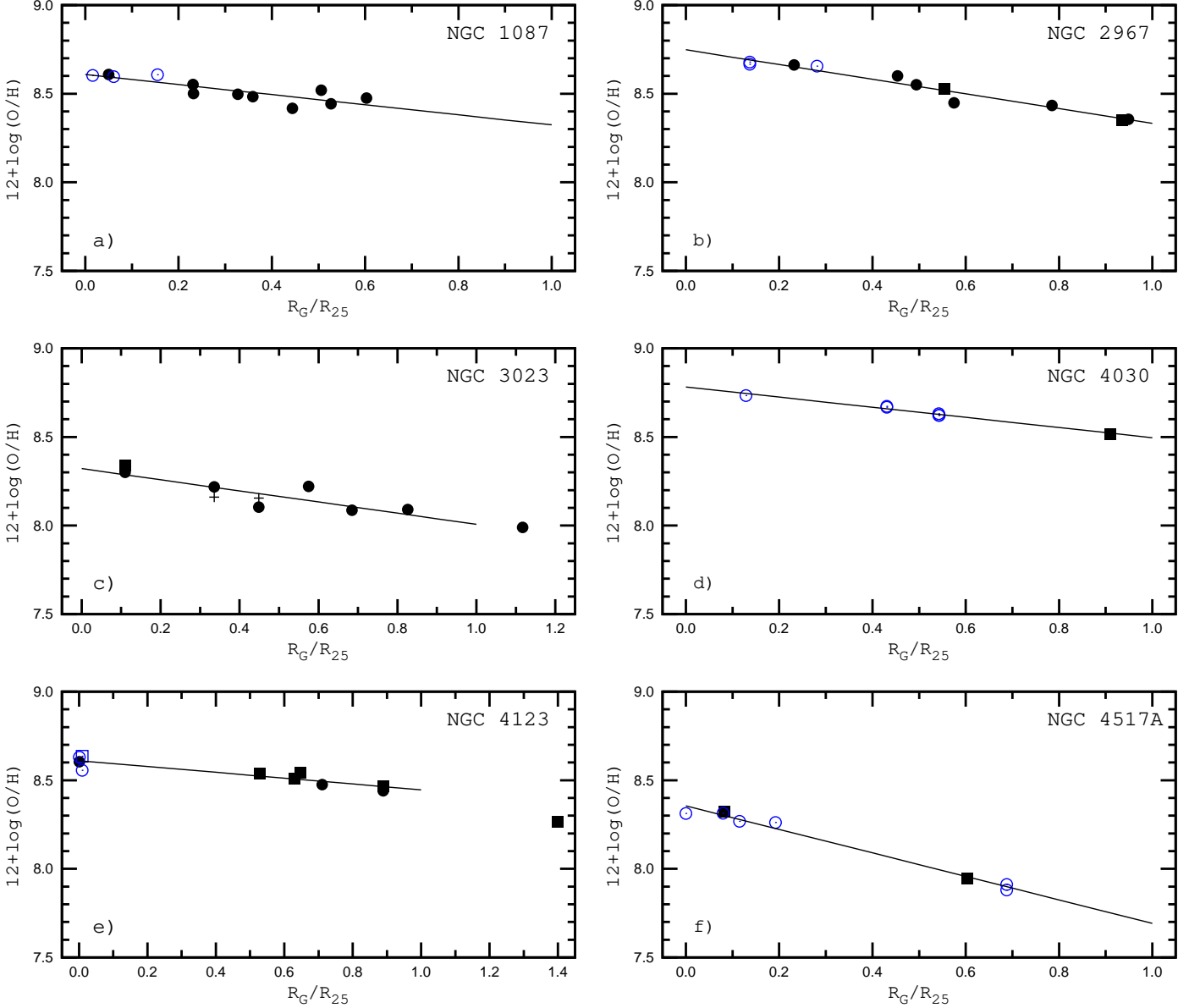


Fig. 8. The radial distributions of oxygen abundances in the disks of our target galaxies. The plus signs are abundances derived through the T_e method, the circles are abundances obtained through the C_{NS} method, and the squares are those inferred through the C_{ON} method. The filled symbols show abundances based on our SALT spectra, the open (blue) symbols are abundances based on spectra from the literature (see text). The solid line in each panel is the best linear fit to the data points with galactocentric distances less than the isophotal R_{25} radius. (A color version of this figure is available in the online version.)

the number of the fiber on the plate.) Since *SDSS* data release 10 (DR10, Ahn et al. 2014) reported line measurements in one spectrum only, we used the *SDSS* spectra from DR7. The oxygen $(\text{O}/\text{H})_{C_{\text{NS}}}$ abundances inferred using the *SDSS* spectra are shown by the open (blue) circles in panel *a* of Fig. 8.

The best linear fit to all the data points (12 points) with galactocentric distances smaller than the isophotal R_{25} radius is

$$12 + \log(\text{O}/\text{H}) = 8.61 \pm 0.02 - 0.285 \pm 0.056 \times (R/R_{25}), \quad (4)$$

with a mean deviation of 0.034 dex around the relationship. The obtained relation is shown by a solid line in panel *a* of Fig. 8.

NGC 2967. The strong lines $\text{H}\beta$, $[\text{O III}]\lambda\lambda 4959, 5007$, $\text{H}\alpha$, $[\text{N II}]\lambda\lambda 6548, 6584$ and $[\text{S II}]\lambda\lambda 6717, 6731$ were measured in six red spectra. Oxygen $(\text{O}/\text{H})_{C_{\text{NS}}}$ abundances were then inferred for those H II regions. These abundances are shown by the filled circles in panel *b* of Fig. 8. The strong lines $[\text{O II}]\lambda\lambda 3727, 3729$,

$\text{H}\beta$, $[\text{O III}]\lambda\lambda 4959, 5007$, $\text{H}\alpha$, and $[\text{N II}]\lambda 6584$ were measured in two blue spectra of H II regions in the galaxy NGC 2967 and were used to estimate oxygen $(\text{O}/\text{H})_{C_{\text{ON}}}$ abundances. Those abundances are shown by the black filled squares in panel *b* of Fig. 8. The obtained oxygen abundances are given in Table 5.

There are three *SDSS* spectra (Sp 476-52314-622, Sp 266-51630-387, and 266-51602-394) of H II regions in the galaxy NGC 2967 in DR7. The oxygen $(\text{O}/\text{H})_{C_{\text{NS}}}$ abundances derived using the *SDSS* spectra are shown by the gray (blue) open circles in panel *b* of Fig. 8.

The best linear fit to all the data points (11 points) with galactocentric distances smaller the isophotal R_{25} radius is

$$12 + \log(\text{O}/\text{H}) = 8.75 \pm 0.02 - 0.414 \pm 0.030 \times (R/R_{25}), \quad (5)$$

Table 5. Oxygen abundances in the H II regions in the disks of our sample of galaxies

Slit	R/R_{25}	$12+\log(\text{O}/\text{H})^a$	Method	spectrum
NGC 1087				
15	0.527	8.44	C_{NS}	red
16	0.359	8.48	C_{NS}	red
17	0.232	8.50	C_{NS}	red
23	0.050	8.61	C_{NS}	red
28	0.327	8.50	C_{NS}	red
30	0.506	8.52	C_{NS}	red
31	0.231	8.55	C_{NS}	red
32	0.444	8.42	C_{NS}	red
36	0.603	8.48	C_{NS}	red
NGC 2967				
14	0.232	8.66	C_{NS}	red
17	0.554	8.53	C_{ON}	blue
23	0.454	8.60	C_{NS}	red
28	0.575	8.45	C_{NS}	red
29	0.494	8.55	C_{NS}	red
33	0.936	8.35	C_{ON}	blue
37	0.785	8.44	C_{NS}	red
39	0.949	8.36	C_{NS}	red
NGC 3023				
08	0.449	8.16	T_e	blue
		8.10	C_{NS}	red
12	0.336	8.16	T_e	blue
		8.22	C_{NS}	red
14	0.110	8.34	C_{ON}	blue
		8.30	C_{NS}	red
18	0.665	8.09	C_{NS}	red
19	0.575	8.22	C_{NS}	red
21	0.826	8.09	C_{NS}	red
22	1.117	7.99	C_{NS}	red
NGC 4030				
46	0.910	8.52	C_{ON}	blue
NGC 4123				
6	0.001	8.60	C_{NS}	red
14	0.528	8.54	C_{ON}	blue
18	0.711	8.47	C_{NS}	red
20	0.629	8.51	C_{ON}	blue
21	0.646	8.54	C_{ON}	blue
22	0.889	8.44	C_{NS}	blue
		8.47	C_{ON}	blue
26	1.399	8.26	C_{ON}	blue
NGC 4517A				
44	0.603	7.95	C_{ON}	blue
56	0.082	8.32	C_{ON}	blue

^aThe standard error for the C-based methods is around 0.1 dex. See Section 5.1 for more details.

with a mean deviation of 0.026 dex around the relationship. The resulting relation is represented by a solid line in panel *b* of Fig. 8.

NGC 3023. The auroral line $R = [\text{O III}]\lambda 4363$ was detected in two blue spectra of H II regions in the disk of NGC 3023. The oxygen abundances in those H II regions were determined through the direct T_e method. Those abundances are shown by the plus signs in panel *c* of Fig. 8. The strong lines $[\text{O II}]\lambda\lambda 3727, 3729$, $\text{H}\beta$, $[\text{O III}]\lambda\lambda 4959, 5007$, $\text{H}\alpha$, and $[\text{N II}]\lambda 6548$ were measured in one blue spectrum. We derived the oxygen $(\text{O}/\text{H})_{C_{\text{ON}}}$ abundance, finding the total nitrogen flux N_2 to be 4 $[\text{N II}]\lambda 6548$. This abundance is shown by the black filled square in panel *c* of Fig. 8. The strong lines $\text{H}\beta$, $[\text{O III}]\lambda\lambda 4959, 5007$, $\text{H}\alpha$, $[\text{N II}]\lambda\lambda 6548, 6584$

and $[\text{S II}]\lambda\lambda 6717, 6731$ were measured in seven red spectra and used to infer the oxygen $(\text{O}/\text{H})_{C_{\text{NS}}}$ abundance for those H II regions. The total nitrogen fluxes were determined to be $N_2 = 1.33[\text{N II}]\lambda 6584$. Those abundances are shown by the black filled circles in panel *c* of Fig. 8.

There are four *SDSS* spectra (Sp 480-51989-056, Sp 481-51908-289, Sp 267-51608-384, and Sp 267-51608-389) of H II regions in the galaxy NGC 3023. Since there is a large discrepancy between the line fluxes reported in DR7 and DR10 these *SDSS* spectra were not used.

The best linear fit to the data points (9 points) with galactocentric distances smaller than the isophotal R_{25} radius is

$$12 + \log(\text{O}/\text{H}) = 8.32 \pm 0.04 - 0.315 \pm 0.078 \times (R/R_{25}), \quad (6)$$

with a mean deviation of 0.047 dex around the relationship. The obtained relation is plotted by a solid line in panel *c* of Fig. 8.

NGC 4030. Unfortunately, the spectral setup used for this galaxy covers the wavelengths of the $\text{H}\alpha$ and $[\text{N II}]\lambda 6584$ lines only for one of the slits. Therefore, the strong lines $[\text{O II}]\lambda\lambda 3727, 3729$, $\text{H}\beta$, $[\text{O III}]\lambda\lambda 4959, 5007$, $\text{H}\alpha$, and $[\text{N II}]\lambda 6584$ were measured in only one blue spectrum of an H II region in the galaxy NGC 4030. The oxygen $(\text{O}/\text{H})_{C_{\text{ON}}}$ abundance was estimated using the measured strong lines. The inferred abundance is shown by the black filled squares in panel *d* of Fig. 8. There are six *SDSS* spectra (Sp 285-51930-042, Sp 285-51663-044, Sp 285-51930-049, Sp 285-51663-058, Sp 331-52368-405, and Sp 2892-54552-293) of H II regions in the galaxy NGC 4030 in DR7. The oxygen $(\text{O}/\text{H})_{C_{\text{NS}}}$ abundances based on the *SDSS* spectra are shown by the gray (blue) open circles in panel *d* of Fig. 8.

The best linear fit to all the data points (7 points) with galactocentric distances smaller the isophotal R_{25} radius is

$$12 + \log(\text{O}/\text{H}) = 8.78 \pm 0.01 - 0.286 \pm 0.017 \times (R/R_{25}), \quad (7)$$

with a mean deviation of 0.009 dex from the relationship. The relation is shown by a solid line in panel *d* of Fig. 8.

NGC 4123. The strong lines $[\text{O II}]\lambda\lambda 3727, 3729$, $\text{H}\beta$, $[\text{O III}]\lambda\lambda 4959, 5007$, $\text{H}\alpha$, and $[\text{N II}]\lambda 6584$ were measured in five blue spectra of H II regions in the galaxy NGC 4123. The oxygen $(\text{O}/\text{H})_{C_{\text{ON}}}$ abundances based on those spectral data are shown by the black filled squares in panel *e* of Fig. 8. The sulfur lines $[\text{S II}]\lambda\lambda 6717, 6731$ were also measured in the blue spectrum of one H II region in the galaxy NGC 4123. This allowed us to obtain the oxygen $(\text{O}/\text{H})_{C_{\text{NS}}}$ abundance for this particular H II region. The strong lines $\text{H}\beta$, $[\text{O III}]\lambda\lambda 4959, 5007$, $\text{H}\alpha$, $[\text{N II}]\lambda\lambda 6548, 6584$ and $[\text{S II}]\lambda\lambda 6717, 6731$ were measured in two red spectra. The inferred oxygen $(\text{O}/\text{H})_{C_{\text{NS}}}$ abundances are shown by the black filled circles in panel *e* of Fig. 8. It should be noted that the H II region at the center of NGC 4123 (Slit 06) is located close to the line dividing AGNs and star-forming regions in the BPT classification diagram.

Spectra of the region near the center of the NGC 4123 were observed by Kehrig et al. (2004) and by the *SDSS* (Sp 517-52024-504). We obtained abundances of $12+\log(\text{O}/\text{H})_{C_{\text{NS}}} = 8.56$ and $12+\log(\text{O}/\text{H})_{C_{\text{ON}}} = 8.63$ using the spectral measurements of Kehrig et al. (2004). Moreover, we measured an abundance of $12+\log(\text{O}/\text{H})_{C_{\text{NS}}} = 8.63$ using the DR10 line fluxes.

The best linear fit to all the data points (10 points) with galactocentric distances smaller than the isophotal R_{25} radius is

$$12 + \log(\text{O}/\text{H}) = 8.61 \pm 0.01 - 0.164 \pm 0.025 \times (R/R_{25}), \quad (8)$$

with a mean deviation of 0.025 dex. This relation is represented by a solid line in panel *e* of Fig. 8.

NGC 4517A. The strong lines $[\text{O II}]\lambda\lambda 3727, 3729$, $\text{H}\beta$, $[\text{O III}]\lambda\lambda 4959, 5007$, $\text{H}\alpha$, and $[\text{N II}]\lambda 6584$ were measured in the blue spectrum of an H II region in the galaxy NGC 4517A. In another spectrum, the line $[\text{N II}]\lambda 6584$ is out of our spectral range, but the line $[\text{N II}]\lambda 6548$ is included. We derived the oxygen $(\text{O}/\text{H})_{\text{O3N2}}$ abundance in these spectra. The total nitrogen flux N_2 was determined to be $N_2 = 1.33[\text{N II}]\lambda 6584$ in the former case and to be $N_2 = 4[\text{N II}]\lambda 6548$ in the latter case. These abundances are shown by the black filled squares in panel *f* of Fig. 8.

Romanishin et al. (1983) reported emission-line ratios $[\text{S II}](\lambda 6717 + \lambda 6731)/\text{H}\alpha$, $\text{H}\alpha/[\text{N II}](\lambda 6548 + \lambda 6584)$, and $[\text{O III}](\lambda 4959 + \lambda 5007)/\text{H}\beta$ obtained from photographic spectra of four H II regions in NGC 4517A. We estimated the oxygen $(\text{O}/\text{H})_{\text{CSN}}$ and nitrogen $(\text{N}/\text{H})_{\text{CSN}}$ abundances from those strong lines. Romanishin et al. (1983) did not provide the positions of the observed H II regions, but listed the deprojected radii instead. We corrected these galactocentric distances for the galaxy distance adopted here and used the resulting values. Furthermore, there are two SDSS spectra (Sp 289-51990-627 and Sp 290-51941-350) of H II regions in NGC 4517A. The abundances based on the SDSS and Romanishin et al.'s data are shown by the gray (blue) open circles in panel *f* of Fig. 8.

The best linear fit to all the data points (8 points) with galactocentric distances smaller than the isophotal R_{25} radius is

$$12 + \log(\text{O}/\text{H}) = 8.35 \pm 0.01 - 0.663 \pm 0.033 \times (R/R_{25}), \quad (9)$$

with a mean deviation of 0.023 dex. This relation is indicated by a solid line in panel *f* of Fig. 8.

5.4. Comparison between the distributions of the abundances determined through the *C* method and via the O3N2 and N2 calibrations

Many calibrations based on photoionization models or/and H II regions with abundances determined through the direct T_e -method were suggested for nebular abundance determinations (Pagel et al. 1979; Alloin et al. 1979; Dopita & Evans 1986; McGaugh 1991; Zaritsky et al. 1994; Pilyugin 2000, 2001; Kewley & Dopita 2002; Pettini & Pagel 2004; Pilyugin & Thuan 2005; Tremonti et al. 2004; Stasińska 2006, among many others). The discrepancies between metallicities of a given H II region derived using different calibrations can be large, up to ~ 0.6 dex (see reviews by Kewley & Ellison 2008; López-Sánchez & Esteban 2010; López-Sánchez et al. 2012). However, one would expect that all the calibrations based on the abundances in H II regions determined through the T_e method should produce the abundances close to each other. Since the *C* method produces abundances on the same metallicity scale as the T_e -method those abundances should be close to the abundances produced by other calibrations based on the direct abundances in H II regions.

The O3N2 and N2 calibrations suggested by Pettini & Pagel (2004) are widely used. The original O3N2 and N2 calibrations are hybrid calibrations, i.e., they are based on both H II regions with abundances determined through the direct T_e -method and photoionization models. ‘‘Pure’’ empirical O3N2 and N2 calibrations (i.e., based on H II regions with abundances determined through the direct T_e -method) were recently presented by Marino et al. (2013). Thus we determined the $(\text{O}/\text{H})_{\text{O3N2}}$ abundances in our H II regions also using the O3N2 calibration of Marino et al. (2013)

$$12 + \log(\text{O}/\text{H})_{\text{O3N2}} = 8.533 - 0.214 \times \text{O3N2} \quad (10)$$

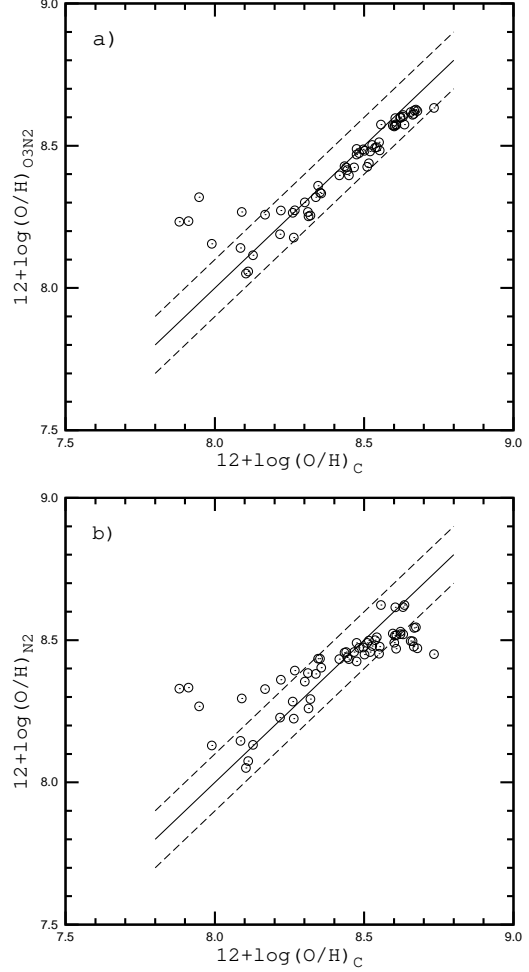


Fig. 10. Comparison of the oxygen abundances in the individual H II regions of our sample determined through the *C* method with oxygen abundances obtained through the O3N2 calibration (upper panel) and through the N2 calibration (lower panel). The solid line indicates a one-to-one correspondence. The dashed lines are shifted by ± 0.1 dex.

where $\text{O3N2} = \log\left(\frac{[\text{O III}]\lambda 5007/\text{H}\beta}{[\text{N II}]\lambda 6584/\text{H}\alpha}\right)$, and the $(\text{O}/\text{H})_{\text{N2}}$ abundances using their N2 calibration

$$12 + \log(\text{O}/\text{H})_{\text{N2}} = 8.743 + 0.462 \times \text{N2} \quad (11)$$

where $\text{N2} = \log([\text{N II}]\lambda 6584/\text{H}\alpha)$.

Fig. 9 shows the comparison of the radial distributions of the oxygen abundances in the disks of our target galaxies determined through the *C* method (filled dark (black) circles), via the O3N2 calibration (open grey (red) circles), and through the N2 calibration (plus signs). The solid line in each panel is the best linear fit to the $(\text{O}/\text{H})_{\text{C}}$ abundances (the same as in Fig. 8).

Fig. 10 shows the comparison of the oxygen abundances in the individual H II regions of our sample determined through the *C* method with the oxygen abundances obtained through the O3N2 calibration (upper panel) and through the N2 calibration (lower panel).

Fig. 9 and Fig. 10 demonstrate that the $(\text{O}/\text{H})_{\text{O3N2}}$ abundances are in satisfactory agreement (within 0.1 dex) with the $(\text{O}/\text{H})_{\text{C}}$ abundances for H II regions with metallicities $12 + \log(\text{O}/\text{H}) \gtrsim 8.1$. However, a small systematic difference (around 0.05 dex) between $(\text{O}/\text{H})_{\text{O3N2}}$ and $(\text{O}/\text{H})_{\text{C}}$ abundances seems to exist; in the sense that the $(\text{O}/\text{H})_{\text{O3N2}}$ abundances

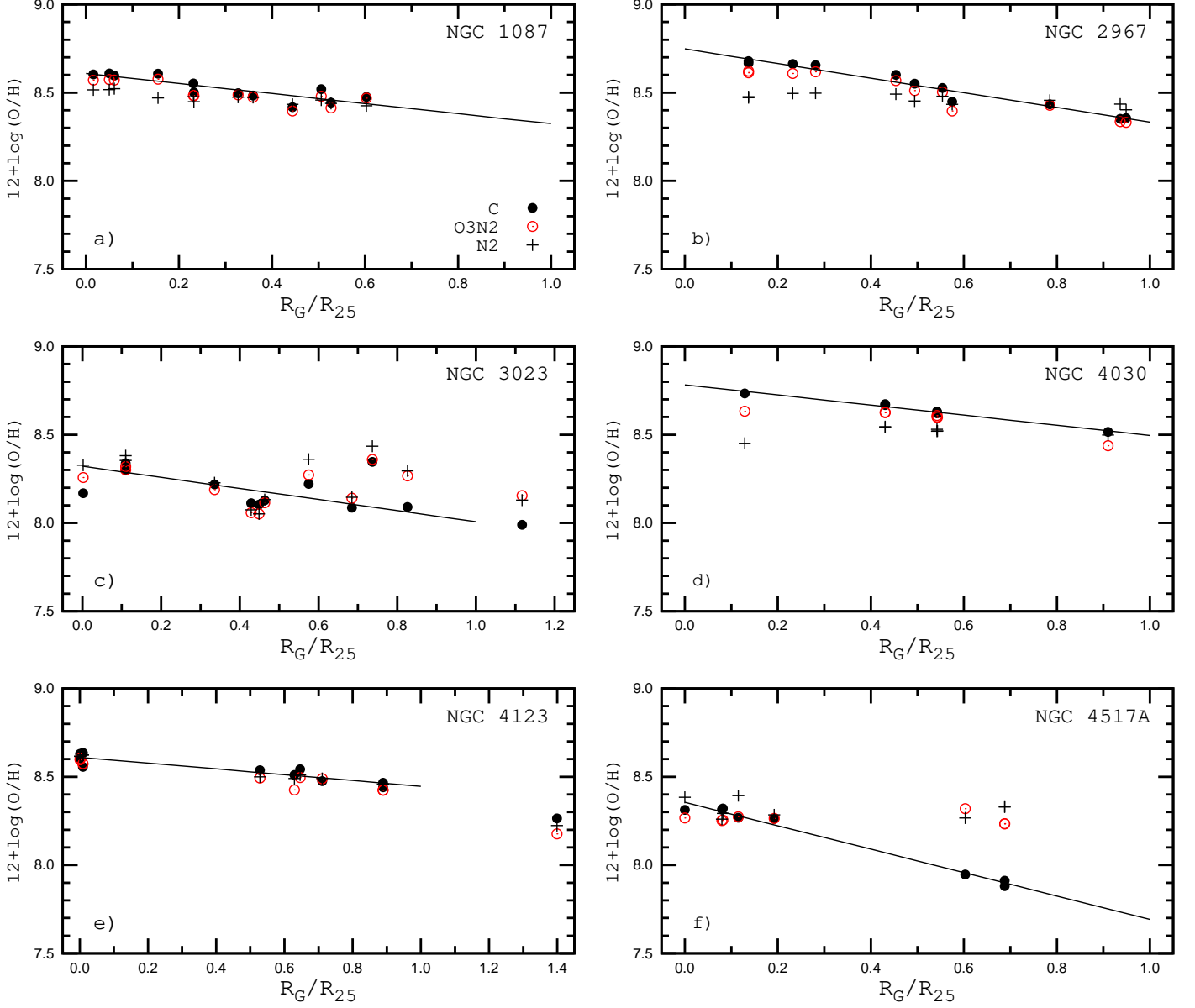


Fig. 9. Comparison of the radial distributions of oxygen abundances in the disks of our target galaxies determined through the C method (filled dark (black) circles), via the $O3N2$ calibration (open grey (red) circles), and through the $N2$ calibration (plus signs). The solid line in each panel is the best linear fit to the $(O/H)_C$ abundances (the same as in Fig. 8). (A color version of this figure is available in the online version.)

are slightly lower than the $(O/H)_C$ abundances. A large disagreement between $(O/H)_{O3N2}$ and $(O/H)_C$ abundances for H II regions with metallicities $12+\log(O/H)_C \lesssim 8.1$ is not surprising since the $O3N2$ calibration of Marino et al. (2013) is constructed for H II regions with metallicities $12+\log(O/H) \gtrsim 8.1$ and does not work at low metallicities. The differences between the $(O/H)_{N2}$ and $(O/H)_C$ abundances exceed 0.1 dex for some H II regions with metallicities $12+\log(O/H) \gtrsim 8.1$. This may suggest that the $O3N2$ calibration of Marino et al. (2013) provides more reliable abundances than their $N2$ calibration.

In summary, the comparison between C -, $O3N2$ -, and $N2$ -based abundances in our target H II regions allows us to suggest that the uncertainties in the obtained $(O/H)_C$ abundances are within ~ 0.1 dex. This supports our estimation of the uncertainties in the abundances discussed in Subsection 5.2.

6. Discussion

The radial distributions of the oxygen abundances across the disks of all the galaxies of our sample are well fitted by linear relationships within the isophotal radius (with the abundances on the logarithmic scale). The mean deviation from the relationship is less than 0.05 dex for each galaxy. The values of the radial abundance gradient vary by a factor of ~ 4 among the galaxies of our sample; from -0.164 dex R_{25}^{-1} for NGC 4123 to -0.663 dex R_{25}^{-1} for NGC 4517A.

The correlation between the local oxygen abundance and the stellar surface brightness (OH – SB relation) or surface mass density has been discussed in many studies (Webster & Smith 1983; Edmunds & Pagel 1984; Vila-Costas & Edmunds 1992; Ryder 1995; Moran et al. 2012; Rosales-Ortega et al. 2012; Sánchez et al. 2014). In our previous paper (Pilyugin et al. 2014b) we examined the relations between the oxygen abun-

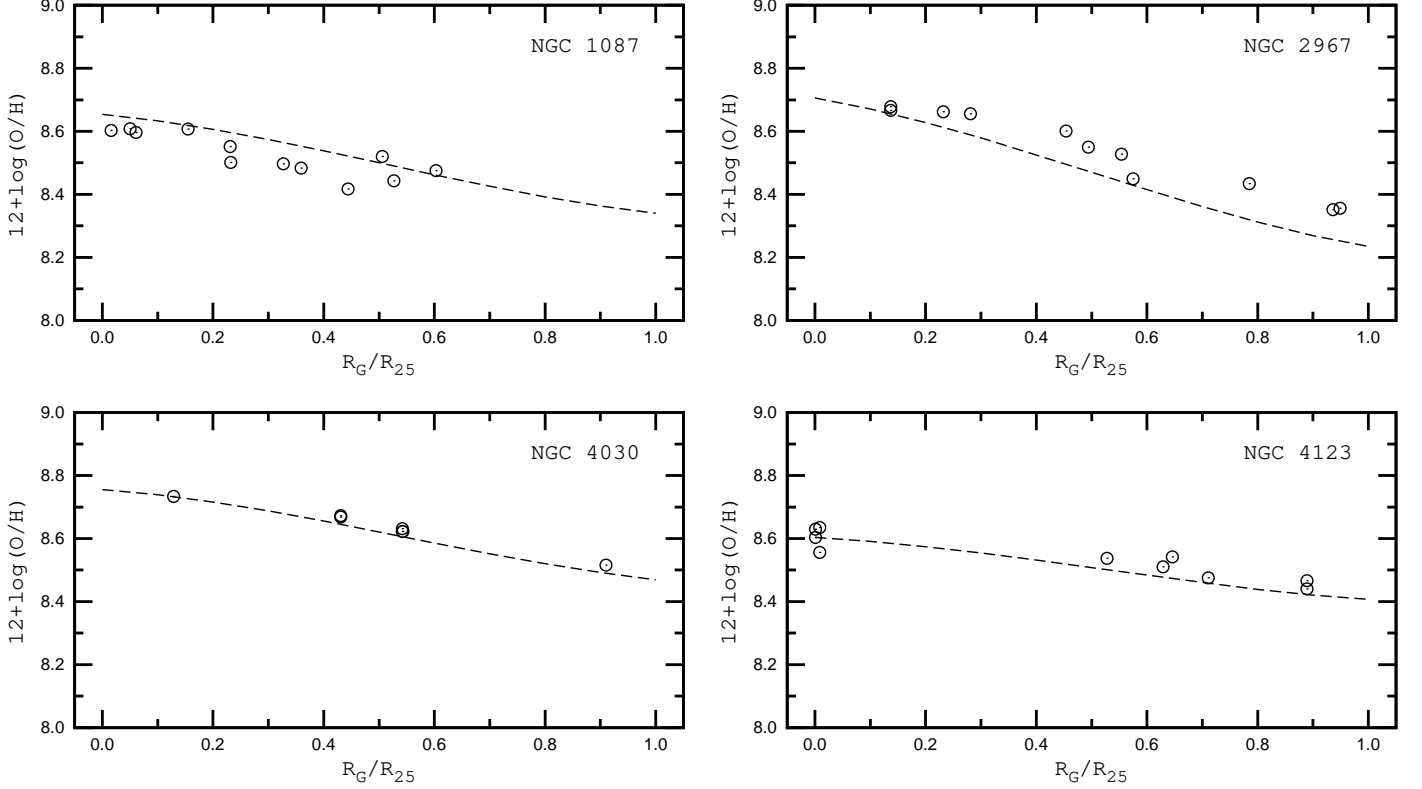


Fig. 11. Radial distributions of oxygen abundances in the disks of the spiral galaxies of our sample. The circles represent the abundances of the individual H II regions (the same as in Fig. 8). The line in each panel shows the abundance distribution predicted by the relation between abundance and surface brightness in the $W1$ band, Eq. (12).

dance and the disk surface brightness in the infrared $W1$ band of *WISE* at different fractions of the optical isophotal radius R_{25} . We found evidence that the $\text{O/H} - SB$ relation varies with galactocentric distance and depends on the disk scale length and the morphological T -type of a galaxy. We derived a general parametric relation between abundance and surface brightness in the $W1$ band, $\text{O/H} = f(SB)$ for spiral galaxies of type $Sa - Sd$,

$$\begin{aligned}
 12 + \log(\text{O/H}) = & 7.732 + 0.303x + 0.290x^2 \\
 & + (0.288 + 0.120x \\
 & \quad - 0.139x^2) \log(\Sigma_{LW1})_x \\
 & + (0.0418 - 0.0323x - 0.0022x^2) h_{W1} \\
 & - (0.0122 + 0.0404x + 0.0088x^2) T
 \end{aligned} \quad (12)$$

where $x = r/R_{25}$ is the fractional radius expressed in terms of the isophotal radius of a galaxy (R_{25}), $(\Sigma_L)_x$ is the disk surface brightness, h_{W1} the radial disk scale length, and T the morphological T -type. It is interesting to compare the radial distributions of oxygen abundances predicted by this relationship to the radial abundance trends traced by the oxygen abundances in the H II regions in the disks of our sample of galaxies.

Fig. 11 shows the comparison between the radial distributions of the oxygen abundances predicted by the $\text{O/H} = f(SB)$ relation, Eq. (12), and the abundances obtained from the analysis of the emission-line spectra of H II regions for four of our galaxies, NGC 1087, NGC 2967, NGC 4030, and NGC 4123. The $\text{O/H} = f(SB)$ relation cannot be applied to the other two galaxies of our sample. It was noted above that we could not determine a reliable disk scale length h_{W1} and surface brightness at the center of the disk of the galaxy NGC 3023 since the disk contribution to the surface brightness is close to the observed surface-brightness profile over a small range of radial distances

only (see lower panel of Figure 5). NGC 4517A is a *Sdm* galaxy (with morphological type $T = 8$) whereas the $\text{O/H} = f(SB)$ relation was derived for spiral galaxies of the types $Sa - Sd$ (i.e., for a range of morphological types from $T \sim 1$ to $T \sim 7$).

Inspection of Fig. 11 shows that the oxygen abundances predicted by the parametric $\text{O/H} = f(SB)$ relation are rather close to the abundances obtained from the analysis of the emission-line spectra of H II regions of the galaxies of the present sample where the $\text{O/H} - SB$ relation is applicable. The discrepancy usually does not exceed 0.1 dex. Thus, the parametric $\text{O/H} = f(SB)$ relation can be used for a rough estimation of the oxygen abundances in the disks of spiral galaxies.

Summary

Spectra of H II regions in six late-type galaxies were observed with the South African Large Telescope (SALT). The auroral line $[\text{O III}]\lambda 4363$ was detected in two spectra. The T_e -based oxygen $(\text{O/H})_{T_e}$ abundances in these two H II regions were derived using the equations of the standard T_e -method. The oxygen abundances of the other H II regions were estimated from strong emission lines through the recently suggested “counterpart” method (C method). When the strong lines R_3 , N_2 , and S_2 were measured in our spectra, oxygen $(\text{O/H})_{C_{NS}}$ abundances could be obtained. When, on the other hand, the strong lines R_2 , R_3 , and N_2 were available then oxygen $(\text{O/H})_{C_{ON}}$ abundances were determined. Moreover, we also inferred oxygen abundances of the H II regions in our target galaxies with available spectral measurements from the literature or from the *SDSS* spectroscopic data base through the C method.

We derived oxygen abundances from the individual one-pixel-wide spectra and considered the variations in those abun-

dances. The abundances determined with the C method from the individual one-pixel-wide spectra are close to each other and are close to the abundances obtained from the integrated seven-pixel-wide spectrum. This can be considered as supporting evidence for the robustness and precision of the C -based abundances, which are independent of the area in the H II region image that is measured. In other words, the C method produces a reliable oxygen abundance even if a spectrum of only a part of an H II region is used.

We also determined the $(\text{O}/\text{H})_{\text{O3N2}}$ and $(\text{O}/\text{H})_{\text{N2}}$ abundances in our target H II regions using the O3N2 and N2 calibrations of Marino et al. (2013). The $(\text{O}/\text{H})_{\text{O3N2}}$ abundances are in satisfactory agreement (within 0.1 dex) with the $(\text{O}/\text{H})_C$ abundances for H II regions with metallicities $12+\log(\text{O}/\text{H}) \gtrsim 8.1$. However, a small systematic difference (around 0.05 dex) between $(\text{O}/\text{H})_{\text{O3N2}}$ and $(\text{O}/\text{H})_C$ abundances seems to exist in the sense that the $(\text{O}/\text{H})_{\text{O3N2}}$ abundances are slightly lower than the $(\text{O}/\text{H})_C$ abundances. The differences between the $(\text{O}/\text{H})_{\text{N2}}$ and $(\text{O}/\text{H})_C$ abundances are larger than 0.1 dex for some H II regions. This may suggest that the O3N2 calibration of Marino et al. (2013) provides more reliable abundances than their N2 calibration.

We determined the abundance gradients in the disks of our six late-type target galaxies. The radial distributions of the oxygen abundances across the disks of all the galaxies of our sample are well fitted by linear relationships within the isophotal radius (with abundances on a logarithmic scale). The mean deviation from the relationship is less than 0.05 dex for each galaxy. The values of the radial abundance gradient vary by a factor of ~ 4 among the galaxies of our sample, i.e., from -0.164 dex R_{25}^{-1} for NGC 4123 to -0.663 dex R_{25}^{-1} for NGC 4517A.

We derived surface-brightness profiles in three photometric bands (the $W1$ band of *WISE* and the g and r bands of the *SDSS*) for each galaxy using publicly available photometric imaging data. The characteristics of the disks (the surface brightness at the disk center and the disk scale length) were found through bulge-disk decomposition. Using the photometric parameters of the disks, the oxygen abundance distributions were estimated from the relation between abundance and surface brightness of the disk in the $W1$ band, $\text{O}/\text{H} = SB$, which had been obtained for spiral galaxies in our previous study. The oxygen abundances predicted by the $\text{O}/\text{H} = SB$ relation are rather close to the abundances determined from the analysis of the emission-line spectra of the H II regions in the galaxies of the present sample where the $\text{O}/\text{H} - SB$ relation is applicable. The discrepancy is usually not larger than 0.1 dex. Thus, the parametric $\text{O}/\text{H} = f(SB)$ relation can be used for a rough estimation of the oxygen abundances in the disks of spiral galaxies.

Acknowledgements

The observations reported in this paper were obtained with the Southern African Large Telescope (SALT). L.S.P., I.A.Z., and E.K.G. acknowledge support within the framework of Sonderforschungsbereich (SFB 881) on “The Milky Way System” (especially subproject A5), which is funded by the German Research Foundation (DFG). L.S.P. and I.A.Z. thank the Astronomisches Rechen-Institut at the Universität Heidelberg where this investigation was carried out for the hospitality. A.Y.K. acknowledges the support from the National Research Foundation (NRF) of South Africa. This work was partly funded by the subsidy allocated to the Kazan Federal University for the state assignment in the sphere of scientific activities (L.S.P.).

The authors acknowledge the work of the *SDSS* collaboration. Funding for *SDSS*-III has been provided by the Alfred P. Sloan Foundation, the Participating Institutions, the National Science Foundation, and the U.S. Department of Energy Office of Science. The *SDSS*-III web site is <http://www.sdss3.org/>. *SDSS*-III is managed by the Astrophysical Research Consortium for the Participating Institutions of the *SDSS*-III Collaboration including the University of Arizona, the Brazilian Participation Group, Brookhaven National Laboratory, University of Cambridge, Carnegie Mellon University, University of Florida, the French Participation Group, the German Participation Group, Harvard University, the Instituto de Astrofísica de Canarias, the Michigan State/Notre Dame/JINA Participation Group, Johns Hopkins University, Lawrence Berkeley National Laboratory, Max Planck Institute for Astrophysics, Max Planck Institute for Extraterrestrial Physics, New Mexico State University, New York University, Ohio State University, Pennsylvania State University, University of Portsmouth, Princeton University, the Spanish Participation Group, University of Tokyo, University of Utah, Vanderbilt University, University of Virginia, University of Washington, and Yale University.

We acknowledge the usage of the HyperLeda database (<http://leda.univ-lyon1.fr>).

References

- Abazajian, K. N., Adelman-McCarthy, J. K., Agüeros, M. A., et al. 2009, *ApJS*, 182, 543
- Ahn, C. P., Alexandroff, R., Allende Prieto, C., et al. 2014, *ApJS*, 211, 17
- Ahn, C. P., Alexandroff, R., Allende Prieto, C., et al. 2012, *ApJS*, 203, 21
- Allain, D., Collin-Souffrin, S., Joly, M., & Vigroux, L. 1979, *A&A*, 78, 200
- Baldwin, J. A., Phillips, M. M., & Terlevich, R. 1981, *PASP*, 93, 5
- Blanton, M. R. & Roweis, S. 2007, *AJ*, 133, 734
- Buckley, D. A. H., Swart, G. P., & Meiring, J. G. 2006, *SPIE*, 6267
- Burgh, E. B., Nordsieck, K. H., Kobulnicky, H. A., et al. 2003, *SPIE*, 4841, 1463
- Cardelli, J. A., Clayton, G. C., & Mathis, J. S. 1989, *ApJ*, 345, 245
- Crawford, S. M., Still, M., Schellart, P., et al. 2010, *SPIE*, 7737, 54
- de Vaucouleurs, G., de Vaucouleurs, A., Corwin, Jr., H. G., et al. 1991, Third Reference Catalogue of Bright Galaxies (Springer-Verlag Berlin Heidelberg New York)
- Dopita, M. A. & Evans, I. N. 1986, *ApJ*, 307, 431
- Edmunds, M. G. & Pagel, B. E. J. 1984, *MNRAS*, 211, 507
- Fouqué, P., Gourgoulhon, E., Chamaraux, P., & Paturel, G. 1992, *A&AS*, 93, 211
- García, A. M. 1993, *A&AS*, 100, 47
- Izotov, Y. I., Thuan, T. X., & Lipovetsky, V. A. 1994, *ApJ*, 435, 647
- Karachentsev, I. D. 1972, *Soobshcheniya Spetsial'noj Astrofizicheskoy Observatorii*, 7, 1
- Kauffmann, G., Heckman, T. M., Tremonti, C., et al. 2003, *MNRAS*, 346, 1055
- Kehrig, C., Telles, E., & Cuisinier, F. 2004, *AJ*, 128, 1141
- Kewley, L. J. & Dopita, M. A. 2002, *ApJS*, 142, 35
- Kewley, L. J., Dopita, M. A., Sutherland, R. S., Heisler, C. A., & Trevena, J. 2001, *ApJ*, 556, 121
- Kewley, L. J. & Ellison, S. L. 2008, *ApJ*, 681, 1183
- Kniazev, A. Y. 2012, *Astronomy Letters*, 38, 707
- Kniazev, A. Y., Pustilnik, S. A., Grebel, E. K., Lee, H., & Pramskij, A. G. 2004, *ApJS*, 153, 429
- Kobulnicky, H. A., Nordsieck, K. H., Burgh, E. B., et al. 2003, *SPIE*, 4841, 1634
- López-Sánchez, Á. R., Dopita, M. A., Kewley, L. J., et al. 2012, *MNRAS*, 426, 2630
- López-Sánchez, Á. R. & Esteban, C. 2010, *A&A*, 517, A85
- Marino, R. A., Rosales-Ortega, F. F., Sánchez, S. F., et al. 2013, *A&A*, 559, A114
- McGaugh, S. S. 1991, *ApJ*, 380, 140
- Micheva, G., Östlin, G., Zackrisson, E., et al. 2013, *A&A*, 556, A10
- Moran, S. M., Heckman, T. M., Kauffmann, G., et al. 2012, *ApJ*, 745, 66
- O'Donoghue, D., Buckley, D. A. H., Balona, L. A., et al. 2006, *MNRAS*, 372, 151
- Pagel, B. E. J., Edmunds, M. G., Blackwell, D. E., Chun, M. S., & Smith, G. 1979, *MNRAS*, 189, 95
- Paturel, G., Fouqué, P., Bottinelli, L., & Gougouenheim, L. 1989, *A&AS*, 80, 299
- Paturel, G., Petit, C., Prugniel, P., et al. 2003, *A&A*, 412, 45
- Pettini, M. & Pagel, B. E. J. 2004, *MNRAS*, 348, L59

- Pilyugin, L. S. 2000, *A&A*, 362, 325
Pilyugin, L. S. 2001, *A&A*, 369, 594
Pilyugin, L. S., Grebel, E. K., & Kniazev, A. Y. 2014a, *AJ*, 147, 131
Pilyugin, L. S., Grebel, E. K., & Mattsson, L. 2012, *MNRAS*, 424, 2316
Pilyugin, L. S., Grebel, E. K., Zinchenko, I. A., & Kniazev, A. Y. 2014b, *AJ*, 148, 134
Pilyugin, L. S. & Thuan, T. X. 2005, *ApJ*, 631, 231
Pilyugin, L. S. & Thuan, T. X. 2007, *ApJ*, 669, 299
Pilyugin, L. S., Vílchez, J. M., Cedrés, B., & Thuan, T. X. 2010a, *MNRAS*, 403, 896
Pilyugin, L. S., Vílchez, J. M., & Thuan, T. X. 2010b, *ApJ*, 720, 1738
Romanishin, W., Strom, K. M., & Strom, S. E. 1983, *ApJS*, 53, 105
Rosales-Ortega, F. F., Sánchez, S. F., Iglesias-Páramo, J., et al. 2012, *ApJ*, 756, L31
Ryder, S. D. 1995, *ApJ*, 444, 610
Sánchez, S. F., Rosales-Ortega, F. F., Iglesias-Páramo, J., et al. 2014, *A&A*, 563, A49
Schlafly, E. F. & Finkbeiner, D. P. 2011, *ApJ*, 737, 103
Schlegel, D. J., Finkbeiner, D. P., & Davis, M. 1998, *ApJ*, 500, 525
Stasińska, G. 2006, *A&A*, 454, L127
Storey, P. J. & Zeippen, C. J. 2000, *MNRAS*, 312, 813
Thuan, T. X., Pilyugin, L. S., & Zinchenko, I. A. 2010, *ApJ*, 712, 1029
Tremonti, C. A., Heckman, T. M., Kauffmann, G., et al. 2004, *ApJ*, 613, 898
van Dokkum, P. G. 2001, *PASP*, 113, 1420
Vila-Costas, M. B. & Edmunds, M. G. 1992, *MNRAS*, 259, 121
Webster, B. L. & Smith, M. G. 1983, *MNRAS*, 204, 743
Weiner, B. J., Williams, T. B., van Gorkom, J. H., & Sellwood, J. A. 2001, *ApJ*, 546, 916
Wright, E. L., Eisenhardt, P. R. M., Mainzer, A. K., et al. 2010, *AJ*, 140, 1868
Zaritsky, D., Kennicutt, Jr., R. C., & Huchra, J. P. 1994, *ApJ*, 420, 87